Properties of M 2 O 3 /Au(111) Honeycomb Monolayers (M = Sc, Ti, V, Cr, Mn, Fe, Co, Ni)

J. Goniakowski, C. Noguera

Properties of M_2O_3/Au(111) Honeycomb Monolayers (M = Sc, Ti, V, Cr, Mn, Fe, Co, Ni)

J. Goniakowski* and C. Noguera*

CNRS-Sorbonne Université, UMR 7588, INSP, F-75005 Paris, France

Supporting Information

ABSTRACT: We have used a DFT + U approach to study the characteristics of a series of 3d transition-metal oxide monolayers (MLs) of M_2O_3 stoichiometry (M = Sc, Ti, V, Cr, Mn, Fe, Co, and Ni) in freestanding and Au(111)-supported honeycomb structures. They include Mott–Hubbard (Ti_2O_3, V_2O_3), mixed Mott–Hubbard/charge-transfer (Cr_2O_3, Mn_2O_3, Fe_2O_3, Co_2O_3, and Ni_2O_3), and purely charge-transfer (Sc_2O_3) oxides. We have found that besides a structural polarization, the interaction with the Au substrate induces an interfacial electron transfer and considerably modifies the electronic characteristics of the monolayers. In particular, in Ti_2O_3, V_2O_3, and Ni_2O_3, due to the purely d character of the relevant gap edges, these modifications may be rationalized in terms of a change of the cation oxidation state with respect to the corresponding bulk and freestanding ML reference. We propose a general conceptual framework that links the properties of the separate systems (band offsets and character of the states at the gap edges), the value of the interfacial electron transfer, and the electronic and energetic characteristics of the supported MLs. Our results and analysis furnish guidelines toward the tuning of electronic and magnetic characteristics beyond those imposed by the oxide stoichiometry, of direct interest for modern technologies.

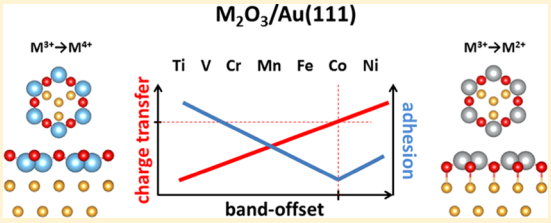

1. INTRODUCTION

Two-dimensional (2D) materials, such as graphene, silicene, germanene, hexagonal boron nitride, or transition-metal dichalcogenides, had been the subject of intense research during the last decade. In parallel to the studies on these 2D van der Waals materials, much progress has also been made in the synthesis and characterization of ultrathin oxide films and in particular oxide monolayers (MLs).[1] In a number of cases, these 2D oxides display a structure reminiscent of graphene, far from a rigid cut of their bulk lattice. Indeed, honeycomb (HC) structures with 6-membered rings have been observed in MgO,[2] ZnO,[3,4] BeO,[5] FeO,[6,7] or CoO[8,9] and with 12-membered rings in monolayers of sesquioxides crystallizing in the corundum structure, such as Ti_2O_3,[10−14] V_2O_3,[15−17] or Nb_2O_3,[18] grown on metal substrates. The same honeycomb structure has also been found in the copper oxide Cu_3O_2 ML, which forms on Au(111).[19]

We have recently shown that the low dimensionality of freestanding M_2O_3 monolayers, associated with their peculiar, perfectly flat atomic structure, is responsible for their specific electronic characteristics—change in the degree of covalency and in the gap width, orbital reconstruction, and new spin ordering compared to their bulk counterparts—and that the same is true for MLs of mixed $MM'O_3$ composition.[20] Since M_2O_3 monolayers cannot be exfoliated, the question arises as to how the specific properties displayed by freestanding MLs are preserved in an experimentally achievable context, that is, when the MLs are deposited/grown on a substrate. Several strategies may be envisioned. For example, systems of $(M_2O_3)_{1,2}/(Al_2O_3)_5$ stoichiometry, with metals M belonging to either the 5d or the 3d transition series, have recently been theoretically considered in a search for potential topological insulators.[21,22] Our focus is rather on metal-supported 2D oxides, which are known to be sensitive to the interaction and the electron exchange with noble metal substrates,[13,23,24] leading to properties that strongly differ from those of their parent materials, either bulk or freestanding thick and ultrathin films.[1,25−29] The most prominent examples include unusual stoichiometries and cation oxidation states[13,30] or the altered stability and electronic structure of point and line defects such as vacancies,[14,31,32] edges,[33,34] etc.

In the present work, we consider the series of Au(111)-supported honeycomb monolayers of M_2O_3 sesquioxides, with M belonging to the 3d transition series (M = Ti, V, Cr, Mn, Fe, and Co). It contains Ti_2O_3 and V_2O_3 oxides of Mott–Hubbard character, whose monolayers have already been synthesized on metal substrates, but includes also oxides of a mixed Mott–Hubbard/charge-transfer character Cr_2O_3, Mn_2O_3, Fe_2O_3, and Co_2O_3. To broaden the perspective toward a case of a purely charge-transfer oxide and an oxide with a particularly large electronic affinity, we also have included Sc_2O_3 and Ni_2O_3 oxides. While the practical fabrication of such supported honeycomb films depends on their thermodynamic stability with respect to other oxide phases under the experimental oxygen conditions and on possible kinetic hindering during their growth, here we focus on the effect of a metal substrate

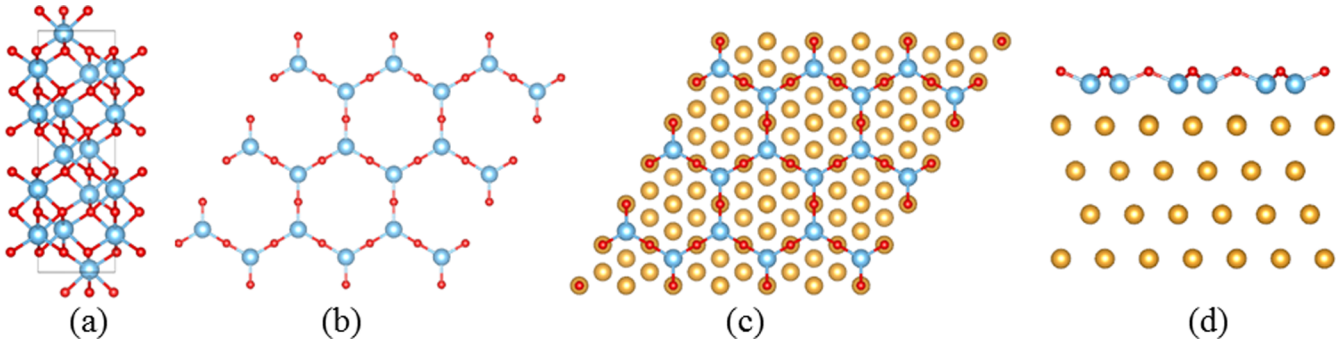

Figure 1. Atomic structures of bulk corundum-like M_2O_3 oxide (a) and of fully relaxed freestanding (b) and Au-supported (c: top view; d: side view) M_2O_3 honeycomb monolayer. Cations, oxygen, and gold atoms are represented by blue, red, and golden balls, respectively.

Table 1. Calculated Characteristics of Au-Supported M_2O_3 MLs (M = Sc, Ti, V, Cr, Mn, Fe, Co, and Ni)[a,b]

	Sc_2O_3	Ti_2O_3	V_2O_3	Cr_2O_3	Mn_2O_3	Fe_2O_3	Co_2O_3	Ni_2O_3
d_{M-O}	1.86	1.81	1.79	1.78	1.69/1.88	1.74/1.77	1.71	1.78
	(1.92)	(1.84)	(1.80)	(1.79)	(1.81)	(1.79)	(1.74)	(1.76)
d_{M-Au}	3.18	2.91	2.86	2.99	3.36/2.89	2.99/2.90	3.17	3.30
Δz	0.84	0.71	0.69	0.62	0.32/0.88	0.53/0.63	0.39	−0.64
misfit	15.4	10.6	8.3	7.8	8.8	7.6	4.7	6.1
Q_M	1.81	2.00	1.84	1.66	1.67/1.47	1.51/1.49	1.39	1.08
	(1.92)	(1.74)	(1.62)	(1.58)	(1.56)	(1.63)	(1.42)	(1.28)
Q_O	−1.00	−1.02	−0.96	−0.94	−0.93	−0.91	−0.88	−0.97
	(−1.28)	(−1.16)	(−1.08)	(−1.06)	(−1.04)	(−1.09)	(−0.95)	(−0.85)
Q_{Au}	−0.64	−0.95	−0.79	−0.50	−0.35	−0.26	−0.12	+0.75
μ_{tot}	0.7	0.0	2.0	5.0	7.2	−0.4	0.0	0.0
μ_M	0.0	0.0	1.2	2.7	3.2/4.3	3.5/−3.7	2.7	1.5
	(0.0)	(0.9)	(2.1)	(2.9)	(4.1)	(3.9)	(2.8)	(1.8)
μ_O	0.3	0.0	−0.1	−0.1	−0.1	−0.1	0.0	0.0
MS	FM	NM	FM	FM	FM	AF	AF	AF
	(NM)	(AF)	(FM)	(AF)	(FM)	(AF)	(AF)	(FM)

[a]Cation−oxygen d_{M-O} and cation−Au d_{M-Au} bond lengths (Å); film rumpling Δz (Å); misfit with respect to Au (%); Bader charges (e) on cations Q_M, oxygen atoms Q_O, and on the gold substrate Q_{Au} (per surface unit-cell); total magnetic moment in the unit cell μ_{tot}; cation and oxygen magnetic moments μ_M and μ_O (μ_B); and ground-state spin order MS. [b]FM and AF denote parallel and antiparallel spin orders, respectively, and NM denotes a nonmagnetic state. Values in parenthesis give the corresponding results for freestanding M_2O_3 MLs.[20]

on their structural, electronic, and magnetic properties. Our results enable us to propose a general conceptual framework that links the properties of the separate systems (band offsets and character of the states at the band edges), the value of the interfacial electron transfer, and the film's electronic (cation charge and magnetic moment) and energetic (adhesion energies) characteristics.

This paper is organized as follows. After a section devoted to the computational method and setup (Section 2), we report the results on Au-supported M_2O_3 MLs with a reference to those on their freestanding counterparts (Section 3). These results are then discussed in Section 4, before a conclusion.

2. COMPUTATIONAL DETAILS

Density functional theory (DFT) calculations were performed with the Vienna ab initio simulation package (VASP)[35,36] using the projector augmented wave method[37,38] to represent the electron−core interaction and a 400 eV energy cutoff in the development of Kohn−Sham orbitals on a plane-wave basis set. The dispersion-corrected (optB88-vdW)[39−41] exchange−correlation functional was employed within the DFT + U approach proposed by Dudarev.[42,43] As in our previous studies,[20,44,45] we have used U values close to those reported in the literature: U = 0 eV for Sc_2O_3, U = 1 eV for Ti_2O_3, U = 1.7 eV for V_2O_3, U = 3 eV for Cr_2O_3 and Fe_2O_3, U = 4 eV for Mn_2O_3 and Co_2O_3, and U = 5 eV for Ni_2O_3. Moreover, we have performed complementary calculations with different U values or using the HSE03 hybrid approach[46,47] to test the sensitivity of our results regarding the choice of the exchange−correlation functional (Section 4.2 and Supporting Information (SI) Section S2). All calculations were spin-polarized, and the relative stability of simple nonmagnetic (NM) and magnetic solutions (with either parallel (FM) or antiparallel (AF) spin moments) was systematically tested. Ionic charges were estimated with the partition scheme proposed by Bader,[48,49] and magnetic moments were obtained by integration of the spin density within the Bader volumes. Atomic configurations were plotted with VESTA.[50]

We have considered Au(111)-supported monolayers of M_2O_3 composition (M = Sc, Ti, V, Mn, Cr, Fe, Co, and Ni) in a honeycomb structure, Figure 1. All of them were modeled in a (2 × 2)-Au(111) unit cell, with a single M_2O_3 formula unit per cell. In all cases, we have found that the oxide cations M preferentially occupy surface hollow sites, whereas oxygen anions are located on top of surface Au atoms. The gold substrate was represented by a slab composed of four (111) atomic layers at the Au experimental bulk lattice parameter of 2.88 Å. The oxide film was deposited on one side of the gold

slab. The sampling of the Brillouin zone was performed with a Γ-centered (14 × 14 × 1) Monkhorst−Pack mesh.[51] The coordinates of all atoms were allowed to fully relax in the direction normal to the gold surface until forces were lower than 0.01 eV $Å^{-1}$.

3. RESULTS

This section presents the computational results on the Au-supported M_2O_3 MLs (M = Sc, Ti, V, Cr, Mn, Fe, Co, and Ni). In Table 1 and in Figures 2−4, we summarize their structural,

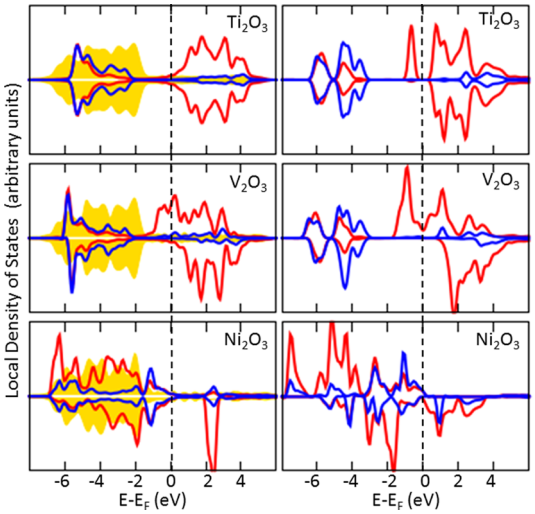

Figure 2. Local densities of states in Au-supported (left) and freestanding (right) M_2O_3 MLs (from top to bottom M = Ti, V, and Ni) projected on cations (red), oxygen atoms (blue), and Au substrate (golden shading). A broadening of 0.2 eV has been systematically applied. The vertical dashed lines indicate the positions of the Fermi levels.

electronic, and magnetic characteristics and compare them with the results obtained for the corresponding freestanding MLs.[20] Excellent agreement is found with electronic structure results obtained using the hybrid exchange−correlation functional, which are given in SI Section S2 and discussed in Section 4.2.

Results in Table 1 show that with respect to the perfectly planar geometry of the freestanding films, the interaction with the gold substrate has two major consequences. First, the supported M_2O_3 MLs display a significant structural polarization, quantified by the vertical separation Δz between the anion and cation atomic planes (rumpling). Its amplitude correlates with that of the misfit between the oxide ML and Au(111) lattices in the series and decreases quasi-monotonically due to a progressive reduction of the cation−oxygen bond length d_{M-O} in the series. The similarity of d_{M-O} in the freestanding and supported films regardless of the lattice misfit proves that the latter is nearly entirely accommodated by the film rumpling Δz. Second, electrons are exchanged between the oxide film and the metal substrate, which develops a charge Q_{Au} (per unit cell). A large electron transfer toward the gold substrate occurs at the beginning of the transition series (M = Sc, Ti, V), weakens progressively for M = Cr, Mn, Fe, and Co, before changing its sign (electrons transferred toward the oxide) in Ni_2O_3/Au. We note the existence of a direct correlation between the signs of the interfacial charge transfer Q_{Au} and of the film polarization Δz, reflecting an electrostatic coupling between them. A thorough discussion of the microscopic mechanisms that are responsible for the nature of the interface charge redistribution and for the strength of the oxide−metal interaction at the oxide/Au interface will be given in the Discussion section.

More specifically, as far as electronic characteristics are concerned, the local densities of states (LDOS) shown in Figures 2−4 and their decomposition into l components (see SI, Figures S1−S3) evidence noticeable modifications upon deposition, including orbital reconstructions (hybridization of d_{z^2}, d_{xz}, and d_{yz} cation orbitals with the Au orbitals) and shifts of states across the Fermi level E_F. From this viewpoint, the eight systems may be split into three groups depending on how their properties are modified upon interaction with Au. The first group includes Ti_2O_3, V_2O_3, and Ni_2O_3 for which substantial electronic modifications take place. The substrate-induced modifications are relatively minor in Sc_2O_3, Cr_2O_3, and Co_2O_3, whereas Mn_2O_3 and Fe_2O_3 represent more complex cases with nonequivalent cations in the unit cell. We describe these three groups in more details in the next sections.

3.1. Ti_2O_3/Au, V_2O_3/Au, and Ni_2O_3/Au. Upon deposition, Ti_2O_3 and V_2O_3 experience a relatively large (more than 0.2*e*) increase of their cation Bader charge Q_M and a substantial (close to 1 μ_B) reduction of their cation magnetic moment μ_M. Their LDOS close to the Fermi level are also strongly modified. In Ti_2O_3/Au, the atomic-like majority peak of d_{z^2} character, characteristic of Ti^{3+} in the freestanding films (see SI, Figure S1), is pushed above the Fermi level and entirely emptied when the film is Au-supported. A similar scenario holds for the majority d_{z^2} peak in V_2O_3/Au. Despite a nonvanishing electron redistribution between majority and minority spin components in the valence band (VB) and the difficulty in assessing oxidation states in a metallic system (at variance with the unquestionable 3+ cation valence in freestanding MLs), the modifications of LDOS, cation charges, and magnetic moments can be rationalized in terms of an increase of the cation oxidation state from M^{+3} in freestanding to M^{+4} in the Au-supported Ti_2O_3 and V_2O_3 films, enabled by a large electron transfer toward the Au substrate ($Q_{Au} \sim -0.95$ and $-0.8e$, respectively) and the Mott−Hubbard character of these oxides.

Interestingly, while the effects are nearly as strong in Ni_2O_3/Au, they act in the opposite way: the electrons are transferred from the metal toward the oxide film ($Q_{Au} = +0.75e$) and the nickel charge Q_M decreases by about 0.2*e*. These changes are associated with a clear reduction of the empty LDOS when the film is supported. Despite the absence of a well-pronounced change of μ_M, this can tentatively be assigned to a reduction of the nickel oxidation state from +3 in the freestanding film to +2 when it is Au-supported.

3.2. Cr_2O_3/Au, Co_2O_3/Au, and Sc_2O_3/Au. In these three systems, characterized by a smaller electron transfer toward Au, the substrate-induced changes of Bader charges Q_M and magnetic moments μ_M are relatively small (less than 0.1*e* and 0.2 μ_B, respectively, Table 1). Q_{Au} is the smallest in Co_2O_3/Au, where it is associated with only a small orbital rehybridization within the VB. Aside from some metal-induced gap states (MIGS) due to the penetration of the gold wave functions in the oxide layer, the oxide insulating character is preserved when the film is deposited on the Au substrate, Figure 3. At variance, the interface charge transfer is relatively large ($Q_{Au} = -0.64e$) in Sc_2O_3/Au, but the transferred electrons are

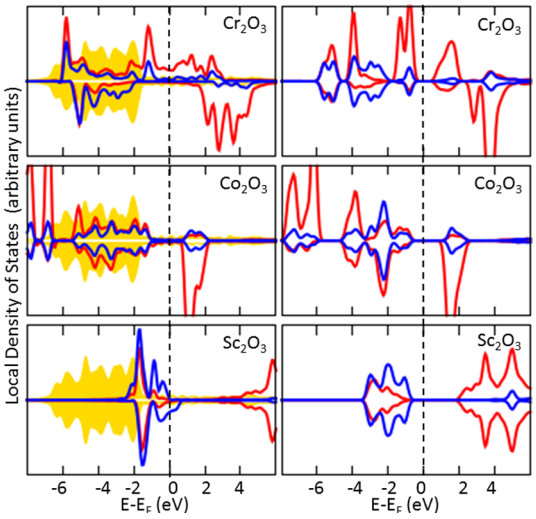

Figure 3. Same as Figure 2, for M = Cr, Co, and Sc.

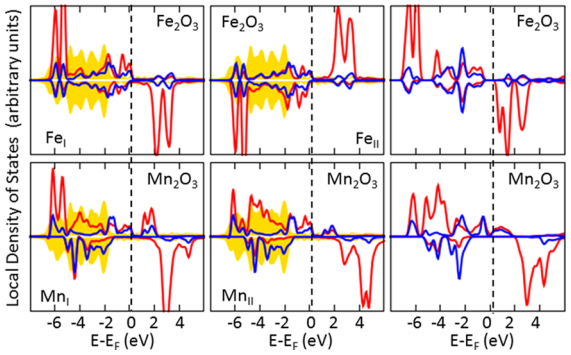

Figure 4. Same as Figure 2, for M = Fe and Mn. Local densities of states (LDOS) of the two inequivalent cations M_I and M_{II} are plotted separately.

principally provided by the anions. The Fermi level enters the top of the VB of purely oxygen character, leading to a decrease of the oxygen charges Q_O by as much as 0.28*e*, Table 1, which is consistent with the purely charge-transfer character of this oxide, Figure 3.

In Cr_2O_3/Au, the Au-induced changes of both Q_{Cr} and μ_{Cr} are weak, but Q_{Au} = 0.50*e* is rather large, and the film LDOS undergoes a significant distortion, which results in a gap closing in the supported film. However, from the l-decomposed LDOS (SI, Figure S2), it appears that despite the substantial LDOS distortion, the occupation of its l components is not significantly altered by the electron exchange with the metal support. Indeed, despite the loss of its atomic-like character typical of the freestanding ML, the majority d_{z^2} orbital remains populated by nearly one electron. Similarly, nearly two electrons remain in the majority $d_{xz} + d_{yz}$ orbitals, which are subject to a less pronounced distortion. A small depopulation of these components visible in SI, Figure S2, is compensated by an equally small increase of occupation of the $d_{x^2-y^2}$ and d_{xy} ones.

3.3. Mn_2O_3/Au and Fe_2O_3/Au. Mn_2O_3/Au and Fe_2O_3/Au constitute more complex cases. In the former, the two Mn cations Mn_I and Mn_{II} (reported in this order in Table 1) display a significant electronic dissimilarity, with substantially different charges (the two Q_{Mn} differ by 0.2*e*) and magnetic moments (the two μ_{Mn} differ by more than 1 μ_B). The LDOS of the two cations are also dissimilar, Figure 4. In particular, the Mn_I majority LDOS, of mainly $d_{x^2-y^2} + d_{xy}$ character (SI, Figure S3), has clearly a larger amplitude in the conduction band (CB). However, since the amplitude of its minority VB LDOS is also much larger, this suggests that the reduction of the Mn_I magnetic moment results from a redistribution of electrons between majority and minority bands, rather than from a change of oxidation state. We will come back to this point in Section 3.4. Interestingly, the electronic Mn differentiation is accompanied by a structural one, with the two Mn−O bond lengths differing by nearly 0.2 Å and the Mn−Au bond lengths by 0.45 Å. A similar structural effect had also been reported in ref 22. and assigned to a Jahn−Teller distortion.

A cation differentiation also takes place in Fe_2O_3/Au, but it is much smaller than in Mn_2O_3/Au. The Bader charges of the two Fe cations differ by 0.02*e* only and their magnetic moments by no more than 0.2 μ_B. The associated structural effects are also small, with Fe−O bond lengths differing by 0.03 Å only and Fe−Au ones by ≈0.1 Å. As far as the two cation LDOS close to the Fermi level are concerned, Figure 4, E_F intercepts the VB of the Fe_I LDOS while it remains located above the VB maximum (VBM) in the Fe_{II} LDOS.

It should be noted that in all oxide MLs, the two cations are not structurally equivalent in the unit cell since one occupies a face-centered cubic and the other an hexagonal close packed site of the Au(111) surface. However, this nonequivalence only leads to tiny differences in charges and magnetic moments, much smaller than in Fe_2O_3 and Mn_2O_3.

3.4. Interfacial Charge Distribution. To assess the spatial characteristics of the interfacial electron redistribution more precisely than the Bader analysis, we depict in Figure 5 the differential electron densities at the M_2O_3/Au(111) interfaces in four cases, representative of a strong (V_2O_3), a complex (Mn_2O_3), a weak (Cr_2O_3), and a reversed (Ni_2O_3) effect of the Au substrate on the cation electronic characteristics. The maps are obtained by subtracting the total electron densities of the separated systems (the bare gold slab and the unsupported oxide film) from that of the constituted one while maintaining all atoms at their positions in the supported configuration. Positive and negative differential densities (red and blue in Figure 5, respectively) correspond to regions that are populated and depopulated upon interface formation.

Despite different amplitudes, symmetries, and signs, the electron redistribution upon deposition displays some features that are common to all these systems. In particular, the differential density maps highlight the existence of density maxima in the interfacial region between the gold substrate and the oxide film, which Bader analysis mainly assigns to surface gold atoms. Indeed, in V_2O_3/Au, Mn_2O_3/Au, and Cr_2O_3/Au (cases of negative Q_{Au}), the maximum differential electron densities are found along the cation−Au bonds in this interfacial region. Consistent with the results and discussion of Table 1, the depopulation of the oxide films, which mainly affects cation orbitals of d_{z^2} character, weakens along the V, Mn, and Cr series. Also, intra-atomic electron rearrangements can be identified (e.g., a depopulation of $d_{x^2-y^2} + d_{xy}$ components coupled to a filling of $d_{xz} + d_{yz}$ ones in V_2O_3). Interestingly, in Mn_2O_3/Au, there is no electron coupling between Mn_I and the gold surface, which supports the interpretation given in the preceding section that the strong reduction of its magnetic moment is not due to the charge

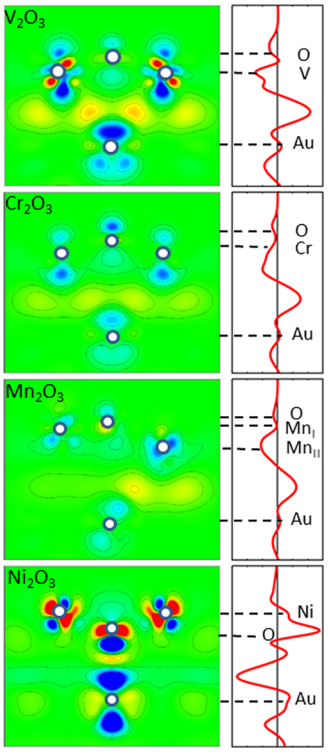

Figure 5. Left: differential density maps of V_2O_3, Cr_2O_3, Mn_2O_3, and Ni_2O_3 MLs supported on Au(111), plotted in the plane perpendicular to the surface and passing through two cations, an oxygen, and a surface Au atom (positions of atoms are indicated with white circles). Electron excess and deficiency are depicted in red and blue, respectively. Right: corresponding integrated differential densities along the direction normal to the Au(111) surface.

transfer toward Au but rather to an intra-atomic electron redistribution.

In the case of Ni_2O_3/Au (positive Q_{Au}), electrons move from the surface Au atoms and from the interfacial region toward the oxide ions. Since the oxygen atoms are in contact with the gold surface (negative rumpling), they are subject to a strong electronic rearrangement, with the maxima of the differential density being indicative of filled O–Au bonding states. An intra-atomic orbital polarization also takes place on oxygen atoms, with an electron transfer from p_z to the $p_x + p_y$ orbitals which are hybridized with Ni orbitals.

To summarize, the interface electron transfer and the substrate-induced effects in the oxide MLs tend to be the most pronounced at the beginning of the transition series and attenuate progressively in its middle and toward its end, before changing sign in the case of Ni_2O_3. The oxide electronic and magnetic characteristics can be rationalized in terms of a change of cation oxidation states in Ti_2O_3, V_2O_3, and Ni_2O_3. The electronic characteristics of the remaining MLs display much weaker changes with respect to those of their freestanding counterparts.

4. DISCUSSION

In this section, we first analyze the mechanisms that drive the modifications of the electronic structure of the M_2O_3 MLs induced by the substrate. Further on, we discuss the sensitivity of our results to the choice of the exchange–correlation functional. Finally, we extend the discussion to the adhesion characteristics of the supported MLs.

4.1. Interfacial Electron Redistribution. To identify the origin of the electron redistribution at M_2O_3/Au interfaces and to link it to the electronic characteristics of the separate constituents (freestanding M_2O_3 film and bare Au(111) surface), we have searched whether the interfacial charge transfer Q_{Au} is correlated to the offset between the metal Fermi level E_F and the oxide point of zero charge E_{ZCP}, as predicted from the MIGS filling at metal/semiconductor interfaces to rationalize the values of the Schottky barrier height.[52−54] Although such a rigid band model is only indicative since additional changes of level positions necessarily take place in response to the electron transfer, it has been proved in the past to give qualitatively reliable results. The existence of such a correlation in our systems is a priori not obvious both because the present oxides are not sp materials but rather highly correlated Mott–Hubbard insulators and because the metal Fermi level sometimes falls in their conduction or valence bands rather than in the band gap.

However, Figure 6 (the corresponding results obtained in hybrid calculations are given in SI, Figure S7), obtained by

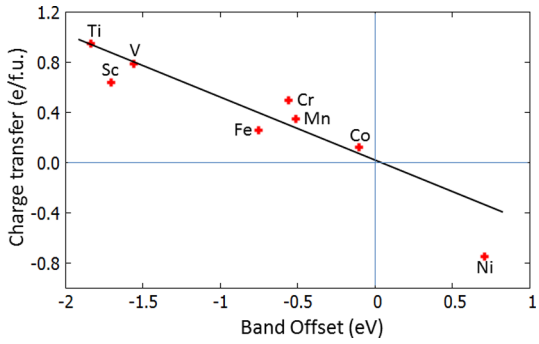

Figure 6. Interface charge transfer Q_{Au} (e) as a function of the offset E_F(Au) − E_{ZCP}(M_2O_3) (eV) between the Fermi level of the bare Au(111) surface and the point of zero charge of the freestanding oxide ML. The line is drawn to guide the eye.

aligning the oxide and substrate vacuum levels and setting E_{ZCP} at midgap, shows a linear relationship between Q_{Au} and the band offset $E_F - E_{ZCP}$. Indeed, we find that the ZCPs progressively shift toward more negative values along the oxide series, following the progressive increase of the metal electronegativity. They are positioned above the Au(111) Fermi level and lead to an electron transfer toward the metal ($Q_{Au} < 0$) in all cases but Ni_2O_3. Positive band offset at the Ni_2O_3/Au interface results in a positive Q_{Au} (electron transfer toward Ni_2O_3), and the different oxide–substrate bonding in this case (reversed rumpling) makes its value deviate somewhat from the common linear relationship. In the extreme opposite limit, large negative $E_F - E_{ZCP}$ values in Sc_2O_3, Ti_2O_3, and V_2O_3 rationalize the strong electron transfer toward the metal substrate found in the full calculations. Finally, band offsets in Cr_2O_3, Mn_2O_3, Co_2O_3, and Fe_2O_3 are much smaller so that only minor charge redistributions are induced by the interaction with the gold substrate. Interestingly, the very same $Q_{Au} \propto E_F - E_{ZCP}$ relationship seems to be respected by systems in which the interface electron exchange provokes substantial changes in the oxide electronic structure (change of the cation oxidation state) as well as by those where these changes are only minor or mainly concern anions.

To get additional insights into the interfacial electron redistribution and to link it to the character of gap edges, we have represented in Figure 7 a band alignment of the eight

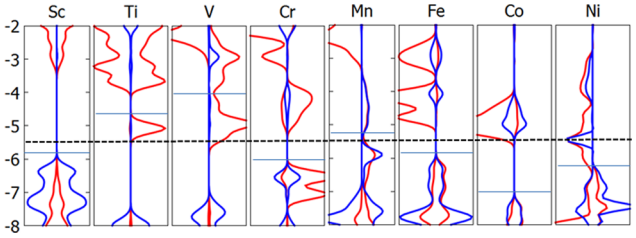

Figure 7. Band alignment of the eight freestanding M_2O_3 MLs with respect to the vacuum level. LDOS projected on cations and oxygen atoms are plotted with red and blue lines, respectively. The oxide Fermi levels (last occupied states) are indicated with thin full lines and that of the bare Au(111) surface is drawn with a thick dashed line.

freestanding M_2O_3 MLs with respect to the vacuum level (the corresponding results obtained by hybrid calculations are given in SI, Figure S8). Our results show that contrary to the behavior of the oxide ZCPs, the positions of the VBM and conduction band minimum (CBm) vary nonmonotonically along the series mostly due to significant differences of gap widths (ranging from 0 to ≈3 eV). Three different generic situations are encountered, fully consistent with the results of the full calculations. In Ti_2O_3/Au and V_2O_3/Au, the oxide valence band maximum (VBM) of purely d character is located largely above the metal Fermi level, which indicates that the electron transfer from the oxide film toward the substrate can provoke an increase of the cation oxidation state to Ti^{4+} and V^{4+}. In Sc_2O_3, the point of zero charge is also located largely above the Au Fermi level, but the purely oxygen character of its VBM prevents any possible change of the cation electronic characteristics. Conversely, in Ni_2O_3/Au, for which the oxide conduction band minimum (CBm) of principally d character is positioned below the metal Fermi level, the electron flow from the metal toward the oxide film can provoke a reduction of the nickel oxidation state to Ni^{2+}. Finally, an electron redistribution essentially due to the filling of the MIGS is expected when the metal Fermi level is located in the oxide band gap, which happens in Sc_2O_3/Au, Cr_2O_3/Au, Mn_2O_3/Au, Fe_2O_3/Au, and Co_2O_3/Au.

In summary, we have shown that the value of the interfacial charge transfer at M_2O_3/Au interfaces and the main features of their electronic structure may be inferred from the positions of the point of zero charge of the freestanding M_2O_3 MLs with respect to the Fermi level of the bare Au surface and from the character of the oxide gap edges. The extreme cases where the oxide VBM of purely d character is positioned well above E_F (Ti_2O_3 and V_2O_3) or its d-like CBm is positioned well below E_F (Ni_2O_3) correspond to large interface charge transfers and to substantial changes of the cation charges/magnetic moments, which were assigned to changes of cation oxidation states.

4.2. Sensitivity to the Exchange–Correlation Functional. Taking into account the well-known difficulty in describing the electronic structure of transition-metal oxides with DFT-based approaches, in this section we discuss the sensitivity of our results to the choice of the exchange–correlation functional. We first compare the DFT + *U* results reported in Section 3 with those obtained from hybrid calculations (summarized in SI). Furthermore, we extend the discussion to the sensitivity of DFT + *U* results to the choice of *U*.

Hybrid electronic structure results have been obtained with the HSE03 exchange–correlation functional implemented in VASP and are displayed in SI, Table S1 and Figures S4–S6. Despite the fundamentally different treatment of exchange effects, the reported DFT + *U* and HSE03 results give very convergent descriptions of the electronic structure of both freestanding and supported HCs. More specifically, for the freestanding MLs, despite slightly larger cation magnetic moments, a somewhat stronger bond ionicity (larger Bader charges), and nearly twice larger gaps in HSE03, both approaches predict very similar characters of the VBM and CBm states and LDOS structures. Moreover, the band alignments of the freestanding MLs with respect to the Fermi level of the Au(111) surface (DFT + *U*: Figure 7; HSE03: SI Figure S7) closely coincide in the two approaches. Similar good consistency was also found for the electronic characteristics of the supported MLs: the cation magnetic moments, the interface charge transfers, and the assignment of cation oxidation states. The single small discrepancy between the two approaches lies in the differentiation between the two Fe cations, which is small in DFT + *U* but absent in HSE03. While such an excellent agreement between the two sets of results additionally validates our findings, one has to remember that HSE03 nevertheless does not provide a fully definitive answer to the electronic characteristics of Mott–Hubbard insulators and that, similar to the Hubbard *U* in the DFT + *U* approach, the percentage of the Hartree–Fock exchange in hybrid methods remains an adjustable parameter, which may not be transferable between bulk materials and freestanding or supported MLs.

To further test the sensitivity of our DFT + *U* results to the choice of the *U* parameters, taking into account the correlation shown in Figure 6, we have first analyzed how the band offsets vary as a function of *U*, Figure 8. We find that the increase of *U*

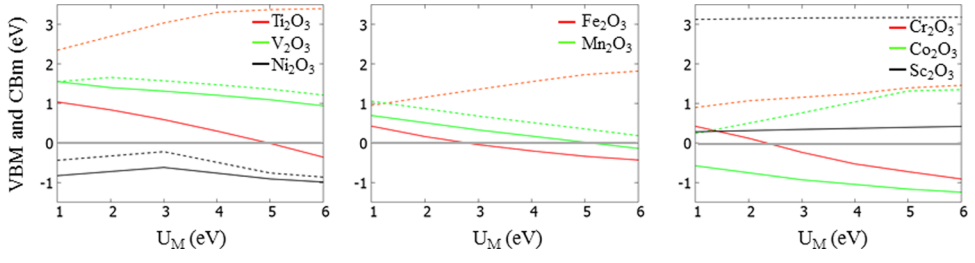

Figure 8. Position of band edges (VBM and CBm represented by full and dashed lines, respectively) in freestanding M_2O_3 films (eV) as a function of *U* (eV) after alignment of their vacuum levels. The zero of energy is fixed at the position of the Au(111) Fermi level (full gray lines).

produces a systematic increase of the band gaps in Ti_2O_3, Fe_2O_3, Cr_2O_3, and Co_2O_3 but has only a minor effect on the gap widths in Sc_2O_3, V_2O_3, Mn_2O_3, and Ni_2O_3 MLs. Among the latter, the VBMs and CBms of V_2O_3 and Mn_2O_3 progressively shift to lower energies as U increases, whereas those of Sc_2O_3 and Ni_2O_3 hardly change position. These behaviors produce a very limited number of cases for which any substantial change of the band offset between the oxide band edges and the Au Fermi level could occur. On the one hand, for (unreasonably) large values of U, the VBM of Ti_2O_3 shifts below the Au(111) Fermi level, suggesting that Ti might remain in its (freestanding-like) 3+ oxidation state. On the other hand, for (unreasonably) small values of U, the VBMs of Fe_2O_3 and Cr_2O_3 move above the metal Fermi level, suggesting a possible occurrence of an M^{4+} state.

We have further analyzed the differences in the cation magnetic moments $\Delta\mu$ between the freestanding and supported MLs, taken as an indication of a change of oxidation state. In Figure 9, we report their sensitivity to the value of U.

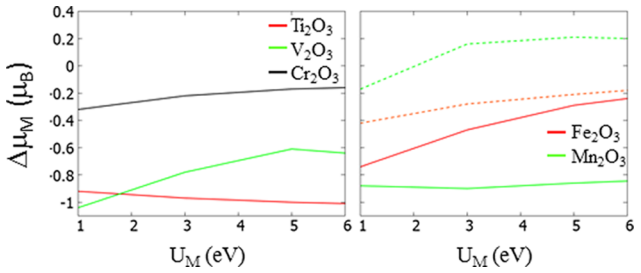

Figure 9. Sensitivity of the changes $\Delta\mu_M$ of cation magnetic moments between supported and freestanding M_2O_3 monolayers to the values of U. Full and dashed lines represent $\Delta\mu_M$ of the two inequivalent cations in Mn_2O_3/Au (green) and Fe_2O_3/Au (red).

To include the most qualitatively different situations, we have chosen Ti_2O_3 and V_2O_3, in which the largest $\Delta\mu$ values were obtained ($\Delta\mu \approx -1$); Cr_2O_3, which is representative of a small $\Delta\mu$; and Mn_2O_3 and Fe_2O_3, in which the two cations bear different magnetic moments, Table 1. In Ti_2O_3 and Cr_2O_3, we find that the magnetic moments are essentially insensitive to the variations of U_{Ti} and U_{Cr}. At variance, $\Delta\mu_V$ in V_2O_3 decreases significantly as U_V increases. In agreement with what is deduced from the band offsets, Figure 8, (unreasonably) large $U_V \gg 6$ eV values would be necessary to recover a magnetic moment close to that in the freestanding layer. Interestingly, while the magnetic moments of Mn_I and Mn_{II} are fairly insensitive to U_{Mn}, the difference between the Fe_I and Fe_{II} μ is enhanced for small $U_{Fe} \sim 1$ eV, but practically suppressed for $U_{Fe} \geq 6$ eV. When compared to the hybrid results, this suggests that the small cation differentiation reported in Section 3 may be due to the slightly too small value of U_{Fe} used in the DFT + U calculations.

A complementary view on the sensitivity of the interface characteristics to the U values is given in Figure 10, which shows that the qualitative correlation between the interfacial charge transfer Q_{Au} and the band offset $E_F(Au) - E_{ZCP}(M_2O_3)$ in the series qualitatively holds irrespective of the U values. However, at a more detailed level, while, in agreement with Figure 8, the band offsets may in some cases (e.g., Mn_2O_3, V_2O_3) vary quite substantially as a function of U, the interface charge transfers are systematically much less sensitive to its precise value.

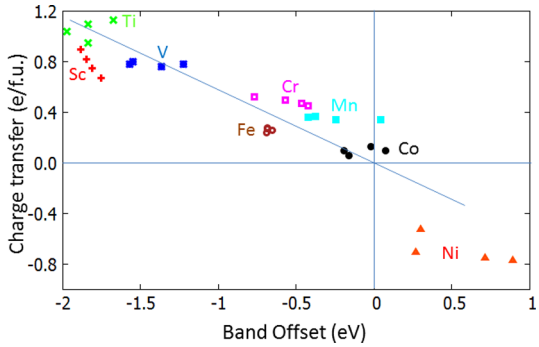

Figure 10. Interface charge transfer Q_{Au} (e) as a function of $E_F(Au) - E_{ZCP}(M_2O_3)$ (eV) for U values ranging from 1 to 6 eV for each oxide. The line is drawn to guide the eye.

In summary, by comparing our present DFT + U results to the corresponding data obtained within the hybrid approximation, and by recording the behavior of oxide and interface electronic characteristics as a function of U, we have shown that the principal conclusions of our study are fairly insensitive to the chosen level of approximation and to the precise computational settings. In particular, this concerns the strong substrate-induced changes of the cation state in Ti_2O_3/Au, V_2O_3/Au, and Ni_2O_3/Au. This also applies to other interface characteristics, such as the interface electron transfer Q_{Au} and its relationship to the offset between the band structures of the separated materials.

4.3. Adhesion at the M_2O_3/Au Interfaces. The adhesion at M_2O_3/Au interfaces may be decomposed into two contributions. The first one is associated with the elastic strain of the freestanding oxide film to match the in-plane lattice parameter of the Au substrate. It depends on the elastic properties of the oxide monolayers and on the misfit between the oxide ML and the Au(111) lattices, but is always unfavorable to adhesion. Our calculations show that despite a relatively large lattice mismatch at the beginning of the series, its value is systematically small (less than 0.5 eV/fu) because the mismatch is principally accommodated by the film rumpling, which involves bending distortions of much lower energies than bond-length modifications.

Accordingly, in the following, we will focus on the second contribution, associated with the direct oxide−metal interaction energy gained when bringing the strained oxide film in contact with the Au(111) substrate. Such separation energy can be estimated from the difference between the total energies of the constituted oxide/metal system and the energy sum of the strained unsupported oxide ML and the bare Au substrate $E^{sep} = -(E_{M_2O_3/metal} - E^{strained}_{M_2O_3} - E_{Au})$. Figure 11 reports the evolution of the separation energy in the M_2O_3/Au series.

We find that E^{sep} spans substantially different values, ranging from particularly large in the case of Ti_2O_3/Au (3.5 eV/fu) to small for Co_2O_3/Au (0.3 eV/fu) and even negative for Sc_2O_3/Au (−0.3 eV/fu). It decreases regularly from Ti_2O_3 to Co_2O_3 and then displays a substantial increase for Ni_2O_3/Au. The Sc_2O_3/Au interface, with negative separation energy, clearly does not follow the common trend, principally due to the large cost of the depopulation of the O-like valence band in this charge-transfer oxide.

While trends in adhesion may not always be easy to rationalize because they involve contributions of various origins, we have tested whether the oxide−metal interaction

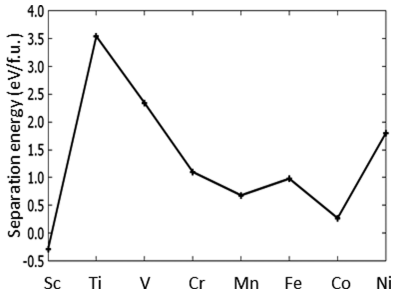

Figure 11. Separation energies E^{sep} (eV per fu) in the series of M_2O_3/Au MLs. The line is drawn to guide the eye.

strength is correlated to the band offset amplitude $|E_F(Au) - E_{ZCP}(M_2O_3)|$ between the metal Fermi level and the oxide point of zero charge. We find that, similar to the behavior of the interface charge transfer, Figure 6, the interface separation energy displays a monotonic increase as a function of $|E_F(Au) - E_{ZCP}(M_2O_3)|$, Figure 12. Interestingly, within the MIGS

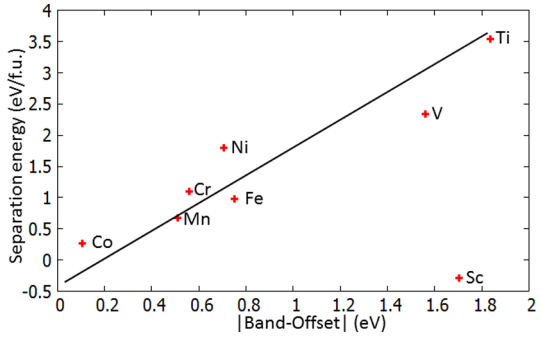

Figure 12. Separation energies E^{sep} (eV/fu) as a function of the absolute value of the offset between the metal Fermi level and the point of zero charge of the freestanding oxide film $|E_F(Au) - E_{ZCP}(M_2O_3)|$ (eV). The line is drawn to guide the eye.

approach,[53,55] the electrostatic energy associated with the interfacial dipole scales as $(E_F(Au) - E_{ZCP}(M_2O_3))^2$. While predictions of the MIGS approach are not necessarily expected to be verified in the present systems, our results show that they nevertheless give a useful guideline to understand the adhesion trends in the M_2O_3 series.

In summary, we have shown that the oxide−metal interaction strength at the M_2O_3/Au interfaces changes substantially along the series, ranging from particularly strong (Ti_2O_3 and V_2O_3) to relatively weak (Mn_2O_3 and Co_2O_3). Similar to the interface charge transfer discussed above, the separation energy is principally driven by the offsets of the band structures of the separate materials, which results in an overall decrease of the interaction strength along the series. Despite a different character of bonding at the interface, the same relationship also holds in the case of interface offset and charge transfer of opposite sign (Ni_2O_3), but it is not obeyed by the purely charge-transfer insulator (Sc_2O_3) due to the large cost of depopulation of the oxygen 2p band.

5. CONCLUSIONS

We have used a DFT + U approach to study the characteristics of a series of 3d transition-metal oxide monolayers of M_2O_3 stoichiometry (M = Sc, Ti, V, Cr, Mn, Fe, Co, and Ni) in freestanding and Au(111)-supported honeycomb structures. Aiming at identifying and rationalizing the trends in the oxide electronic (cation oxidation state), structural (film rumpling), and energetic (film adhesion) characteristics induced by the substrate, we have chosen oxide MLs, which span a wide range of characters, including Mott−Hubbard (Ti_2O_3, V_2O_3), mixed Mott−Hubbard/charge-transfer (Cr_2O_3, Mn_2O_3, Fe_2O_3, Co_2O_3, and Ni_2O_3), and purely charge-transfer (Sc_2O_3) insulators.

We have found that the interaction with the Au substrate considerably modifies the electronic characteristics of Ti_2O_3, V_2O_3, and Ni_2O_3, which may be rationalized in terms of a change of the cation oxidation state (Ti^{4+}, V^{4+}, and Ni^{2+}) with respect to their 3+ state in the corresponding freestanding MLs. In the case of Mn_2O_3, a differentiation between the cations takes place due to an electron redistribution between the majority and minority bands. Conversely, the substrate-induced electronic effects are much less pronounced in Fe_2O_3, Cr_2O_3, and particularly in Co_2O_3. Finally, in the purely charge-transfer Sc_2O_3 oxide, they concern the oxygen atoms rather than the cations.

We have demonstrated that the amplitude of the electron transfer across the oxide/metal interface is driven by the offset between the oxide and gold band structures, which roughly follows the metal electronegativity in the transition series. Moreover, the strong modifications of the cation charges/magnetic moments found in Ti_2O_3/Au, V_2O_3/Au, and Ni_2O_3/Au have been shown to be due to the purely d character of the relevant gap edges and to their positions with respect to the substrate Fermi level.

The adhesion energies at the M_2O_3/Au(111) interfaces vary quasi-monotonically from Ti to Co, principally driven by their direct oxide−metal interaction contributions. Despite a relatively large lattice mismatch at the beginning of the series, the elastic contribution plays a much smaller role because the mismatch is principally accommodated by the film rumpling. Interestingly, similarly to the interfacial electron transfer, the strength of the oxide−metal interaction can also be directly linked to the offset between the oxide band structure and the substrate Fermi level.

Our findings show that due to a significant interface charge redistribution, a metal substrate may enable the stabilization of new cation states, not predictable from the oxide stoichiometry, but of direct interest for modern technologies.

■ ASSOCIATED CONTENT

Supporting Information

The Supporting Information is available free of charge on the ACS Publications website at DOI: 10.1021/acs.jpcc.9b01429.

Numerical results of GGA + U and hybrid (HSE03) calculations performed on: (a) GGA + U: decomposition of cation LDOS for both freestanding and Au-supported oxide honeycombs (Figures S1−S3); (b) HSE03: electronic and magnetic properties of both freestanding and Au-supported oxide honeycombs (Table S1) and LDOS (Figures S4−S6); (c) HSE03: interface charge transfer as a function of band offset (Figure S7) and alignment of the oxide band structures with respect to the Au(111) Fermi level (Figure S8) (PDF)

■ AUTHOR INFORMATION

Corresponding Authors

*E-mail: jacek.goniakowski@insp.jussieu.fr (J.G.).

*E-mail: claudine.noguera@insp.jussieu.fr (C.N.).

ORCID

J. Goniakowski: 0000-0003-4647-9566

C. Noguera: 0000-0002-8665-9695

Notes

The authors declare no competing financial interest.

■ ACKNOWLEDGMENTS

We acknowledge fruitful discussions with M.R. Castell, N. Nilius, S. Surnev, and F.P. Netzer.

■ REFERENCES

(1) *Oxide Materials at the Two-dimensional Limit*; Netzer, F. P.; Fortunelli, A., Eds.; Springer Series in Materials Science; Springer International Publishing: Cham, Switzerland, 2016; Vol. *234*.

(2) Goniakowski, J.; Noguera, C.; Giordano, L. Using polarity for engineering oxide nanostructures: structural phase diagram in free and supported MgO(111) ultrathin films. *Phys. Rev. Lett.* **2004**, *93*, No. 215702.

(3) Claeyssens, F.; Freeman, C. L.; Allan, N. L.; Sun, Y.; Ashfold, M. N.; Harding, J. H. Growth of ZnO thin films-experiment and theory. *J. Mater. Chem.* **2005**, *15*, 139−148.

(4) Tusche, C.; Meyerheim, H. L.; Kirschner, J. Observation of depolarized ZnO(0001) monolayers: formation of unreconstructed planar sheets. *Phys. Rev. Lett.* **2007**, *99*, No. 026102.

(5) Wu, W.; Lu, P.; Zhang, Z.; Guo, W. Electronic and magnetic properties and structural stability of BeO sheet and nanoribbons. *ACS Appl. Mater. Interfaces* **2011**, *3*, 4787−4795.

(6) Ritter, M.; Ranke, W.; Weiss, W. Growth and structure of ultrathin FeO films on Pt(111)studied by STM and LEED. *Phys. Rev. B* **1998**, *57*, 7240−7251.

(7) Ranke, W.; Ritter, M.; Weiss, W. Crystal structures and growth mechanism for ultrathin films of ionic compound materials: FeO(111) on Pt(111). *Phys. Rev. B* **1999**, *60*, 1527−1530.

(8) Gubo, M.; Ebensperger, C.; Meyer, W.; Hammer, L.; Heinz, K. Sub-stoichiometric cobalt oxide monolayer on Ir(100)-(1 × 1). *J. Phys.: Condens. Matter* **2009**, *21*, No. 474211.

(9) Ebensperger, C.; Gubo, M.; Meyer, W.; Hammer, L.; Heinz, K. Substrate-induced structural modulation of a CoO(111) bilayer on Ir(100). *Phys. Rev. B* **2010**, *81*, No. 235405.

(10) Barcaro, G.; Agnoli, S.; Sedona, F.; Rizzi, G. A.; Fortunelli, A.; Granozzi, G. Structure of reduced ultrathin TiO_x polar films on Pt(111). *J. Phys. Chem. C* **2009**, *113*, 5721−5729.

(11) Wu, Q.-H.; Fortunelli, A.; Granozzi, G. Preparation, characterization and structure of Ti and Al ultrathin oxide films on metals. *Int. Rev. Phys. Chem.* **2009**, *28*, 517−576.

(12) Wu, C.; Marshall, M. S. J.; Castell, M. R. Surface structures of ultrathin TiO_x films on Au(111). *J. Phys. Chem. C* **2011**, *115*, 8643−8652.

(13) Wu, C.; Castell, M. R.; Goniakowski, J.; Noguera, C. Stoichiometry engineering of ternary oxide ultrathin films: $Ba_xTi_2O_3$ on Au(111). *Phys. Rev. B* **2015**, *91*, No. 155424.

(14) Wang, S.; Hu, X.; Goniakowski, J.; Noguera, C.; Castell, M. R. Influence of the support on stabilizing local defects in strained monolayer oxide films. *Nanoscale* **2019**, *11*, 2412−2422.

(15) Surnev, S.; Sock, M.; Kresse, G.; Andersen, J. N.; Ramsey, M.; Netzer, F. Unusual CO adsorption sites on vanadium oxide-Pd(111) "inverse model catalyst" surfaces. *J. Phys. Chem. B* **2003**, *107*, 4777−4785.

(16) Guimond, S.; Haija, M. A.; Kaya, S.; Lu, J.; Weissenrieder, J.; Shaikhutdinov, S.; Kuhlenbeck, H.; Freund, H.-J.; Dobler, J.; Sauer, J. Vanadium oxide surfaces and supported vanadium oxide nanoparticles. *Top. Catal.* **2006**, *38*, 117−125.

(17) Feiten, F. E.; Seifert, J.; Paier, J.; Kuhlenbeck, H.; Winter, H.; Sauer, J.; Freund, H.-J. Surface structure of V_2O_3(0001) revisited. *Phys. Rev. Lett.* **2015**, *114*, No. 216101.

(18) Wang, S.; Hu, X.; Goniakowski, J.; Noguera, C.; Castell, M. R. Au-supported Nb_2O_3 honeycomb monolayer films, in preparation.

(19) Möller, C.; Fedderwitz, H.; Noguera, C.; Goniakowski, J.; Nilius, N. Temperature-dependent phase evolution of copper-oxide thin-films on Au(111). *Phys. Chem. Chem. Phys.* **2018**, *20*, 5636−5643.

(20) Goniakowski, J.; Noguera, C. Intrinsic properties of pure and mixed monolayer oxides in the honeycomb structure: M_2O_3 and $MM'O_3$ (M, M′ = Ti, V, Cr, Fe). *J. Phys. Chem. C* **2018**, DOI: 10.1021/acs.jpcc.8b07107.

(21) Afonso, J. F.; Pardo, V. Ab initio study of nontrivial topological phases in corundum-structured $(M_2O_3)/(Al_2O_3)_5$ multilayers. *Phys. Rev. B* **2015**, *92*, No. 235102.

(22) Köksal, O.; Baidya, S.; Pentcheva, R. Confinement-driven electronic and topological phases in corundum-derived 3*d*-oxide honeycomb lattices. *Phys. Rev. B* **2018**, *97*, No. 035126.

(23) Goniakowski, J.; Noguera, C. Polarization and rumpling in oxide monolayers deposited on metallic substrates. *Phys. Rev. B* **2009**, *79*, No. 155433.

(24) Goniakowski, J.; Noguera, C.; Giordano, L.; Pacchioni, G. Adsorption of metal adatoms on FeO(111) and MgO(111) monolayers: Effects of charge state of adsorbate on rumpling of supported oxide film. *Phys. Rev. B* **2009**, *80*, No. 125403.

(25) Jaffe, J. E.; Bachorz, R. A.; Gutowski, M. Band offset and magnetic property engineering for epitaxial interfaces: A monolayer of M_2O_3 (M = Al,Ga,Sc,Ti,Ni) at the α−Fe_2O_3/α−Cr_2O_3 (0001) interface. *Phys. Rev. B* **2007**, *75*, No. 205323.

(26) Freund, H.-J.; Pacchioni, G. Oxide ultra-thin films on metals: new materials for the design of supported metal catalysts. *Chem. Soc. Rev.* **2009**, *37*, 2224−2242.

(27) Nilius, N. Properties of oxide thin films and their adsorption behavior studied by scanning tunneling microscopy and conductance spectroscopy. *Surf. Sci. Rep.* **2009**, *64*, 595−659.

(28) Pacchioni, G.; Freund, H.-J. Electron transfer at oxide surfaces. The MgO paradigm: from defects to ultrathin films. *Chem. Rev.* **2013**, *113*, 4035−4072.

(29) Surnev, S.; Fortunelli, A.; Netzer, F. P. Structure-property relationship and chemical aspects of oxide-metal hybrid nanostructures. *Chem. Rev.* **2013**, *113*, 4314−4372.

(30) Sun, Y.-N.; Giordano, L.; Goniakowski, J.; Lewandowski, M.; Qin, Z.-H.; Noguera, C.; Shaikhutdinov, S.; Pacchioni, G.; Freund, H.-J. The interplay between structure and CO oxidation catalysis on metal- supported ultrathin oxide films. *Angew. Chem., Int. Ed.* **2010**, *49*, 4418−4421.

(31) Giordano, L.; Goniakowski, J.; Pacchioni, G. Properties of MgO(100) ultrathin layers on Pd(100): Influence of the metal support. *Phys. Rev. B* **2003**, *67*, No. 045410.

(32) Prada, S.; Giordano, L.; Pacchioni, G.; Goniakowski, J. Theoretical description of metal/oxide interfacial properties: The case of MgO/Ag(001). *Appl. Surf. Sci.* **2016**, *390*, 578−582.

(33) Goniakowski, J.; Noguera, C.; Giordano, L. Prediction of uncompensated polarity in ultrathin films. *Phys. Rev. Lett.* **2007**, *98*, No. 205701.

(34) Goniakowski, J.; Giordano, L.; Noguera, C. Polarity compensation in low-dimensional oxide nanostructures: the case of metal-supported MgO nanoribbons. *Phys. Rev. B* **2013**, *87*, No. 035405.

(35) Kresse, G.; Furthmuller, J. Efficient iterative schemes for ab initio total energy calculations using a plane-wave basis set. *Phys. Rev. B* **1996**, *54*, 11169−11186.

(36) Kresse, G.; Hafner, J. Ab initio molecular dynamics for liquid metals. *Phys. Rev. B* **1993**, *47*, 558−561.

(37) Blöchl, P. E. Projector augmented-wave method. *Phys. Rev. B* **1994**, *50*, 17953−17979.

(38) Kresse, G.; Joubert, D. From ultrasoft pseudopotentials to the projector augmented-wave method. *Phys. Rev. B* **1999**, *59*, 1758−1775.

(39) Dion, M.; Rydberg, H.; Schroder, E.; Langreth, D. C.; Lundqvist, B. I. Van der Waals density functional for general geometries. *Phys. Rev. Lett.* **2004**, *92*, No. 246401.
(40) Klimeš, J.; Bowler, D. R.; Michaelides, A. Chemical accuracy for the van der Waals density functional. *J. Phys.: Condens. Matter* **2010**, *22*, No. 022201.
(41) Klimeš, J.; Bowler, D. R.; Michaelides, A. Van der Waals density functionals applied to solids. *Phys. Rev. B* **2011**, *83*, No. 195131.
(42) Anisimov, V. I.; Aryasetiawan, F.; Liechtenstein, A. I. First-principles calculations of the electronic structure and spectra of strongly correlated systems: the LDA + U method. *J. Phys.: Condens. Matter* **1997**, *9*, 767−808.
(43) Dudarev, S. L.; Botton, G. A.; Savrasov, S. Y.; Humphreys, C. J.; Sutton, A. P. Electron-energy-loss spectra and the structural stability of nickel oxide: An LSDA + U study. *Phys. Rev. B* **1998**, *57*, 1505−1509.
(44) Le, H.-L. T.; Goniakowski, J.; Noguera, C. Properties of mixed transition metal oxides: $MM'O_3$ in corundum-type structures (M, M′ = Al, Ti, V, Cr, and Fe). *Phys. Rev. Mater.* **2018**, *2*, No. 085001.
(45) Le, H.-L.; Goniakowski, J.; Noguera, C. (0001) Interfaces between M_2O_3 corundum oxides (M = Al, Ti, V, Cr, Fe). *Surf. Sci.* **2019**, *679*, 17−23.
(46) Heyd, J.; Scuseria, G.; Ernzerhof, M. Hybrid functionals based on a screened Coulomb potential. *J. Chem. Phys.* **2003**, *118*, 8207−8215.
(47) Heyd, J.; Scuseria, G.; Ernzerhof, M. Erratum: "Hybrid functionals based on a screened Coulomb potential" [J. Chem. Phys. 118, 8207 (2003)]. *J. Chem. Phys.* **2006**, *124*, 219906.
(48) Bader, R. F. W. A quantum theory of molecular structure and its applications. *Chem. Rev.* **1991**, *91*, 893−928.
(49) Henkelman, G.; Arnaldsson, A.; Jonsson, H. A fast and robust algorithm for Bader decomposition of charge density. *Comput. Mater. Sci.* **2006**, *36*, 354−360.
(50) Momma, K.; Izumi, F. VESTA 3 for three-dimensional visualization of crystal, volumetric and morphology data. *J. Appl. Crystallogr.* **2011**, *44*, 1272−1276.
(51) Monkhorst, H.; Pack, J. Special points for Brillouin-zone integrations. *Phys. Rev. B* **1976**, *13*, 5188−5192.
(52) Flores, F.; Tejedor, C. On the formation of semiconductor interfaces. *J. Phys. C: Solid State Phys.* **1987**, *20*, 145−175.
(53) Bordier, G.; Noguera, C. Electronic structure of a metal-insulator interface: Towards a theory of nonreactive adhesion. *Phys. Rev. B* **1991**, *44*, 6361−6371.
(54) Goniakowski, J.; Noguera, C. Electronic states and schottky barrier height at metal/MgO(100) interfaces. *Interface Sci.* **2004**, *12*, 93−103.
(55) Noguera, C.; Bordier, G. Theoretical approach to interfacial metal-oxide bonding. *J. Phys. III* **1994**, *4*, 1851−1864.